



Fractionation of Solar Wind Minor Ion Precipitation by the Lunar Paleomagnetosphere

A. R. Poppe¹ , I. Garrick-Bethell^{2,3} , and S. Fatemi^{4,5} ¹ Space Sciences Laboratory, University of California at Berkeley, Berkeley, CA 94720, USA; poppe@berkeley.edu² Dept. of Earth and Planetary Sciences, University of California, Santa Cruz, CA, USA³ School of Space Research, Kyung Hee University, Yongin-si, Republic of Korea⁴ Swedish Institute of Space Physics, Kiruna, Sweden⁵ Dept. of Physics, Umeå University, Umeå, Sweden

Received 2020 November 19; revised 2021 February 19; accepted 2021 February 25; published 2021 March 18

Abstract

The analysis of solar wind material implanted within lunar soil has provided significant insight into the makeup and evolutionary history of the solar wind and, by extension, the Sun and protosolar nebula. These analyses often rely on the tacit assumption that the Moon has served as an unbiased recorder of solar wind composition over its 4.5 billion yr lifetime. Recent work, however, has shown that for a majority of its lifetime, the Moon has possessed a dynamo that generates a global magnetic field with surface field strengths of at least $5 \mu\text{T}$. In turn, the presence of such a field has been shown to significantly alter the lunar–solar wind interaction via the formation of a lunar “paleomagnetosphere.” This paleomagnetosphere has implications for the flux of solar wind minor ions to the lunar surface and their subsequent implantation in lunar soil grains. Here we use a three-dimensional hybrid plasma model to investigate the effects of the lunar paleomagnetosphere on the dynamics and precipitation of solar wind minor ions to the lunar surface. The model results show that the lunar paleomagnetosphere can suppress minor ion fluxes to the lunar surface by more than an order of magnitude and strongly fractionates the precipitating solar wind in a complex, nonlinear fashion with respect to both the minor ion charge-to-mass ratio and the surface paleomagnetic field strength. We discuss the implications of these results with respect to both the analysis of trapped material in lunar grains and the semiquantitative $^{40}\text{Ar}/^{36}\text{Ar}$ antiquity indicator for lunar soils.

Unified Astronomy Thesaurus concepts: [The Moon \(1692\)](#); [Lunar magnetic fields \(960\)](#); [Planetary magnetospheres \(997\)](#); [Solar wind \(1534\)](#)

1. Introduction

Examination of lunar regolith samples returned by the Apollo missions has revealed the implantation of exogenous species within the regolith matrix that originate primarily from the solar wind (e.g., Pepin et al. 1970, 1995, 1999; Reynolds et al. 1970; Becker & Clayton 1975; Wieler et al. 1986; Becker & Pepin 1989, 1994; Benkert et al. 1993; Kerridge 1993; Nichols et al. 1994; Wieler 1998), with some additional contributions from terrestrial ionospheric outflow (e.g., Wieler et al. 1999; Ozima et al. 2005; Poppe et al. 2016; Terada et al. 2017; Wei et al. 2020). The analysis of these implanted species has proved to be a critical tool in investigating the detailed composition and evolution of the solar wind both in the present era and as a function of time since the formation of the Moon. Based on the concentrations of implanted species in lunar soils (noble gases, in particular), various analyses have suggested that the overall flux and various isotopic ratios of solar wind elements may have changed over the lifetime of the Sun (see, e.g., Table 1 of Wieler 2016 and references therein), although some of these claims have been challenged by analysis of returned solar wind samples by the Genesis mission (see discussion in Wieler 2016). In particular, Figure 1 shows a synthesis of (a) $^{36}\text{Ar}/^{84}\text{Kr}$ and (b) $^{84}\text{Kr}/^{132}\text{Xe}$ ratios determined from “old” lunar samples, “young” lunar samples, and the Genesis mission, adapted from Wieler (2016). While the observed change of -14% in the $^{36}\text{Ar}/^{84}\text{Kr}$ ratio may be due to

uncertainties and/or biases in the sample analyses, as discussed in Wieler (2016), the $+75\%$ change in the $^{84}\text{Kr}/^{132}\text{Xe}$ ratio has been taken as evidence of a secular change in the elemental fractionation of solar wind Kr and Xe. In addition to inferring solar and solar wind properties from exogenous species, the ratio of $^{40}\text{Ar}/^{36}\text{Ar}$ implanted within lunar samples is a widely used “antiquity” indicator in determining the exposure age of a sample (e.g., Eugster et al. 2001; Joy et al. 2011; Fagan et al. 2014) based on the decaying rate of reimplantation of native lunar atmospheric ^{40}Ar ions (from the radioactive decay of indigenous ^{40}K) into the lunar soil by the solar wind convection electric field (Manka & Michel 1970) and the (heretofore assumed constant) implantation of solar wind ^{36}Ar ions.

One of the fundamental underlying assumptions in the analysis of any exogenous material implanted in lunar soil is that incident ions, whether from the solar wind, terrestrial magnetosphere, or lunar exosphere, have direct access to the lunar surface because of the Moon’s lack of a global magnetic field. With this assumption, the relative atomic and isotopic compositions of material implanted in lunar soil grains can be directly related to the composition of the inflowing plasma, notwithstanding any possible fractionation processes that may occur once the ions have been implanted in the lunar soil, such as depth-dependent fractionation, back-scattering, gas losses by diffusion, and/or cosmic-ray spallation (e.g., Wieler & Baur 1995; Heber et al. 2003; Grimberg et al. 2006; Füri et al. 2020). Over the majority of its ~ 4.5 billion yr history, however, the Moon most likely possessed a dynamo and therefore an intrinsic global magnetic field and associated magnetosphere that may have significantly altered incident plasma fluxes. An extensive body of research has now established that the Moon’s “magnetic history” can be divided into three general

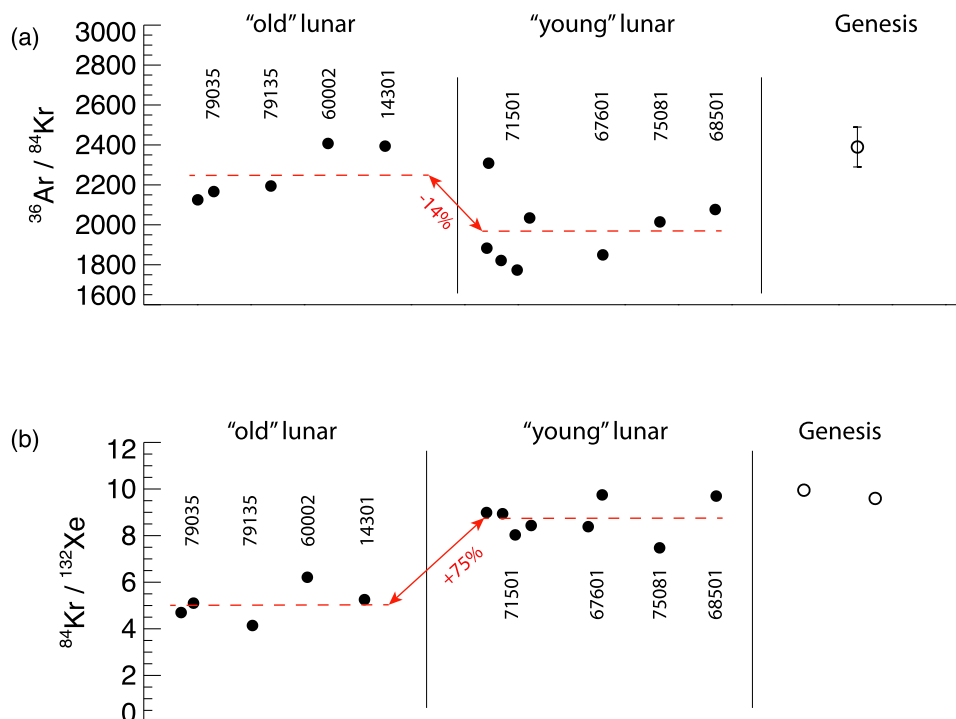


Figure 1. Ratios for (a) $^{36}\text{Ar}/^{84}\text{Kr}$ and (b) $^{84}\text{Kr}/^{132}\text{Xe}$ from Genesis data, “young” lunar samples, and “old” lunar samples, where “young” lunar samples have antiquities less than ~ 100 Ma and “old” lunar samples have antiquities between ~ 1 and 4 Ga (adapted from Wieler 2016). Dashed lines denote median values for each respective subset. A -14% decrease is seen in the $^{36}\text{Ar}/^{84}\text{Kr}$ ratio from “old” to “young” samples, while a $+75\%$ increase is seen in the $^{84}\text{Kr}/^{132}\text{Xe}$ ratio.

epochs: (i) a high-field period, (ii) a low-field (but nonzero) period, and (iii) a zero-field period (e.g., Cisowski et al. 1983; Garrick-Bethell et al. 2009, 2017; Hood 2011; Shea et al. 2012; Tikoo et al. 2014, 2017; Weiss & Tikoo 2014; Baek et al. 2019; Mighani et al. 2020). The high-field epoch occurred early in the Moon’s lifetime between ~ 4.0 and 3.5 Ga with exceedingly strong surface field strengths on the order of 20–100 μT (similar in magnitude to the present-day terrestrial surface field strength of ~ 50 μT). Following the high-field epoch, a low-field epoch persisted between approximately 3.5 and 1.0 Ga with paleomagnetic field strengths on the order of 5 μT (e.g., Tikoo et al. 2017). Finally, by approximately 1 Ga, the lunar dynamo appears to have fully ceased, and surface magnetic field strengths fell to their current-day value near zero (Mighani et al. 2020), leaving behind only patches of remanent crustal magnetic fields distributed heterogeneously across the lunar surface (e.g., Russell et al. 1973; Halekas et al. 2003; Mitchell et al. 2008; Purucker 2008; Garrick-Bethell & Kelley 2019). Despite the uncertainty in dating magnetized lunar samples, the low-field epoch may represent the majority of the Moon’s lifetime (~ 2.5 Gyr in total) and, when taken alongside the high-field epoch as well, suggests that the Moon has possessed a significant global magnetic field for an extended fraction of its lifetime.

Motivated by the findings of Tikoo et al. (2017) that established the lunar low-field paleomagnetic epoch, Garrick-Bethell et al. (2019) investigated the generation of the “lunar paleomagnetosphere” via the use of a three-dimensional hybrid plasma model (*hybrid* refers to the use of fluid electrons and particle ions; see, e.g., Fatemi et al. 2017). This study described both the overall magnetospheric interaction of the lunar paleomagnetosphere with the solar wind and the flux and energy distribution of precipitating protons for surface paleomagnetic field strengths of 0.5, 1, and 2 μT . For all three of these paleomagnetic field strengths, the hybrid model demonstrated the formation of a global paleomagnetosphere that blocked a majority of the solar wind proton flux from reaching

the lunar surface (as expected generally, given our knowledge of Mercury’s global magnetosphere with surface field strengths between ~ 0.3 and 0.7 μT ; e.g., Anderson et al. 2011; Johnson et al. 2012). Despite the overall shielding effect of the global paleomagnetosphere in these cases, Garrick-Bethell et al. (2019) did show that solar wind protons could reach the lunar surface via the magnetospheric cusp regions at locally greater fluxes than in the unmagnetized case, similar to that seen at other bodies with global magnetic fields, such as Mercury and Ganymede (e.g., Massetti et al. 2003; Raines et al. 2014; Poppe et al. 2018; Fatemi et al. 2020; Plainaki et al. 2020). These findings suggest that while there may exist qualitative scaling relations between paleomagnetic field strength and surface ion flux (e.g., stronger paleo fields imply less solar wind flux to the surface), more complex interactions exist within the paleomagnetosphere that locally alter the incident ion flux and energy distributions.

While the model of Garrick-Bethell et al. (2019) focused on the interaction of only solar wind protons with the lunar paleomagnetosphere, other previous work has investigated the interaction of solar wind minor ions with airless bodies in the solar system, both magnetized and unmagnetized. Specifically, Kallio et al. (2008) used a quasi-neutral hybrid model to study the interaction of solar wind H^+ , O^{7+} , and Fe^{9+} ions with Mercury, the Moon, and the asteroid (1) Ceres. In particular, Mercury, with its intrinsic magnetic field and associated magnetosphere, offers an analogy to what one may expect for solar wind minor ion interactions with the lunar paleomagnetosphere—albeit with a much lower magnetic field strength, as Mercury’s surface field strength is ~ 300 nT (notwithstanding the planetary dipole offset; e.g., Johnson et al. 2012), whereas the lunar paleomagnetic field strength during the low-field epoch was ~ 5 μT (Tikoo et al. 2017). In their study, Kallio et al. (2008) found that heavy minor ions (O^{7+} , Fe^{9+}) impacted the surface of Mercury inhomogeneously in somewhat the same manner that protons impacted the surface, although some differences were noted relative to the precipitating proton flux,

Table 1

The Synthetic Ion Names, Masses, Charges, and Charge-to-mass Ratios for the Nine Ion Species Used in the Hybrid Model, Corresponding to the Green Points in Figure 2

Ion Name	Mass [amu]	Charge [e]	Charge-to-mass Ratio
H ⁺	1.00	1	1.00
M ₁ ⁺	2.83	2	0.71
M ₂ ⁺	5.99	3	0.50
M ₃ ⁺	11.3	4	0.35
M ₄ ⁺	19.9	5	0.25
M ₅ ⁺	33.7	6	0.18
M ₆ ⁺	55.6	7	0.13
M ₇ ⁺	89.8	8	0.089
M ₈ ⁺	143.6	9	0.063

meteorites (e.g., Eugster et al. 1969; Hennecke & Manuel 1977; Heber et al. 2001), lunar regolith samples (e.g., Podosek et al. 1971; Wieler et al. 1996), and Genesis mission witness plates (e.g., Vogel et al. 2011; Crowther & Gilmour 2013; Meshik et al. 2014). Thus, their equilibrium charge states in the solar wind are unknown, although Bochsler et al. (2017) predicted Kr charge states of 9–17⁺ and Xe charge states of 7–18⁺, with the most likely charge states being Kr¹⁵⁺ and Xe¹⁴⁺.

For our modeling exercise, we should—strictly speaking—model the behavior of each combination of minor ion mass and charge state in order to fully quantify the variation in ion dynamics and fluxes to the lunar surface. However, as one can quickly determine, this yields far too many combinations to be computationally feasible. Thus, instead of modeling the individual mass and charge state combination for every naturally occurring ion, we instead chose to model protons and eight additional “synthetic” heavy, high charge state minor ions in the solar wind. Each synthetic heavy ion increases in mass and charge state, as shown in green in Figure 2 (the green dots denote the specific charges and masses of the synthetic ions, while the green curves denote the synthetic charge-to-mass ratios) and listed in Table 1. For ease of reference throughout the manuscript, we have denoted the eight synthetic heavy ions as M₁⁺, M₂⁺, ..., M₇⁺, M₈⁺. For the highest masses, we note that the synthetic ions somewhat underestimate the charge states compared to those expected in the solar wind (e.g., the heaviest synthetic ion, M₈⁺, near the mass of Xe has a charge state of only 9⁺, whereas the most likely Xe charge state is 14⁺). However, our synthetic species cover the expected ranges of charge-to-mass ratios as denoted by the green curves in Figure 2; thus, our simulations should capture the relevant physics. (While not presented here, we performed a hybrid model run for a 1 μT paleo field with two different species with identical charge-to-mass ratios, specifically, ⁴He²⁺ and ²⁰Ne¹⁰⁺. The results showed no significant differences between the spatial densities and precipitation flux to the lunar surface between the two heavy ion species, as expected given the q/m scaling in the Lorentz force law.) In the hybrid model, we set the density of all eight heavy minor ion species to be 10⁻⁶ cm⁻³ such that they do not affect the plasma interaction of the core solar wind protons with the lunar paleomagnetic field and act only as “test particles.” Finally, we scaled the temperatures of the heavy minor ions as $T_i \propto m_i$, as has been observed in situ in the solar wind (e.g., Hefti et al. 1998; Bochsler 2007). With these parameters, the upstream thermal gyroradii of the synthetic heavy ions ranged from ~30 (M₁⁺) to ~350 (M₈⁺) km.

All ion species were run with eight particles per cell per species, and all simulations were run for a total of 300 s, equivalent to >7× the time taken for the solar wind to completely transit the simulation domain. This time length, along with visual inspection of the results, ensured that the model came to a steady state before extracting any parameters.

2.1. Caveats and Limitations

Before presenting the model results, we note several limitations and caveats for this study that should be kept in mind. This study has only considered a single set of solar wind conditions and thus does not necessarily address the full range of interactions that may occur. Uncertainty naturally exists in reconstructing the parameters of the solar wind in past epochs (e.g., Airapetian & Usmanov 2016; Ó Fionnagáin & Vidotto 2018; Pognan et al. 2018; Güdel 2020; Oran et al. 2020); thus, our chosen solar wind and interplanetary magnetic field (IMF) values may not be exactly aligned with conditions at ~2 Ga. Additionally, significant variability in the solar wind density and speed, as well as the IMF strength and orientation (e.g., Dmitriev et al. 2011; Jian et al. 2011; McGregor et al. 2011; Wilson et al. 2018), could potentially change some of the details of the solar wind interaction with the lunar paleomagnetosphere. For simplicity, we have also not included the presence of an ~3%–5% contribution from solar wind alpha particles (He⁺⁺), which are the most dominant minor ion in the solar wind (e.g., Bochsler 1987; Aellig et al. 2001; Kasper et al. 2007) and can add additional dynamic pressure to the solar wind. It is possible that extreme, high-pressure solar wind events may deliver solar wind minor ions to the lunar surface in different ratios than quantified here under “typical” solar wind conditions (e.g., as has also been observed and modeled at Mercury; Jia et al. 2019; Slavin et al. 2019; Fatemi et al. 2020). Studies of such extreme solar wind conditions and their effect on the structure of the lunar paleomagnetosphere and solar wind ion precipitation to the lunar surface are identified as future work. We have not considered other orientations for the lunar paleomagnetic field dipole vector, the presence of higher-order magnetic moments (e.g., quadrupole, octupole, etc.), or the possibility of temporal changes (i.e., reorientations) of the lunar dipole over time. A non-spin-aligned orientation for the lunar paleomagnetic field was briefly modeled in Garrick-Bethell et al. (2019) and shown to produce differences in the paleomagnetosphere structure; however, an exploration of the effects of either non-spin-aligned or higher-order magnetic moments is left for future work. When modeling the Moon, we do not include the presence of either crustal magnetic anomalies, which can locally perturb the solar wind flow (e.g., Futaana et al. 2003; Halekas et al. 2006, 2017; Fatemi et al. 2014), or electromagnetically induced fields from conducting layers in the lunar interior (e.g., Grimm & Delory 2012; Fuqua Haviland et al. 2019). Compared to the strength of the global paleomagnetic fields studied here, these perturbations are minor. We do note, for completeness, that under extreme conditions at Mercury, induced fields can be generated with sufficient strength to prevent magnetopause collapse to the surface (e.g., Jia et al. 2015, 2019). At the Moon, by contrast, the much smaller core (i.e., ~2000 km radius at Mercury; ~400 km radius at the Moon) implies that such an effect, while possible, is likely to be much weaker; therefore, such a mechanism can be safely neglected in our simulations. We also do not consider ion backscattering (e.g.,

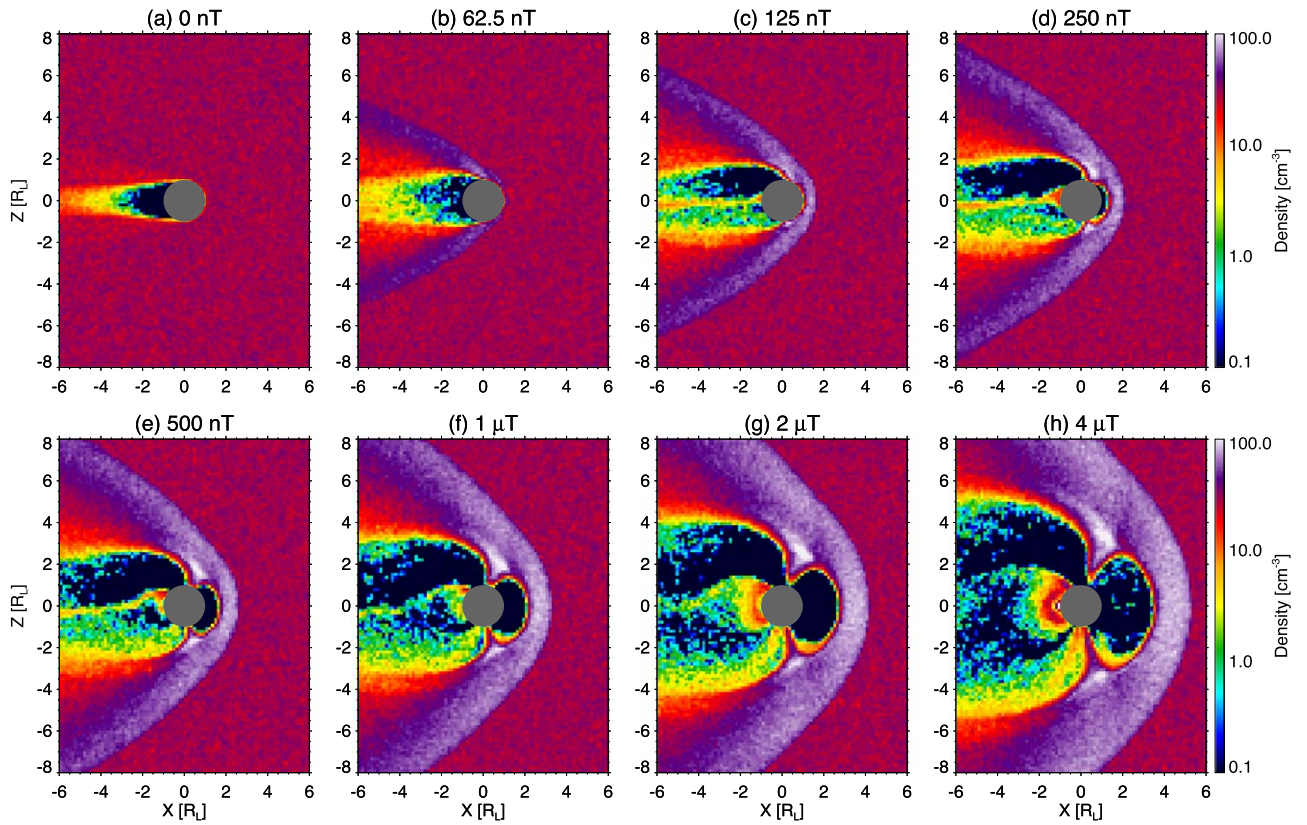


Figure 3. Proton density in the x - z plane for all eight paleomagnetic field strengths.

Saito et al. 2008; Lue et al. 2014) or sputtering (e.g., Wurz et al. 2007; Sarantos et al. 2012; Hijazi et al. 2014; Vorburger et al. 2014) from the lunar surface, as we treat the Moon as a perfect particle absorber for simplicity. Finally, we do not consider the presence of lunar exospheric ions generated via ionization of the Moon’s neutral exosphere. Such ions will also interact with the lunar paleomagnetosphere in complex ways but are most likely a minor perturbation to the overall plasma densities. Further studies of exospheric ion interactions within the lunar paleomagnetosphere are nevertheless identified as future work as well.

3. Model Results

3.1. Global Paleomagnetospheric Structure

Figures 3 and 4 show the proton (H^+) density and magnetic field magnitude, respectively, in the x - z plane for all eight paleomagnetic field strengths. In the 0 nT control case, Figures 3(a) and 4(a), the Moon lacks any global magnetization and forms a simple downstream wake due to absorption of solar wind plasma on the upstream lunar hemisphere. In agreement with present-day in situ observations around the Moon (e.g., Halekas et al. 2005, 2014a; Zhang et al. 2014), the plasma density immediately behind the Moon falls by several orders of magnitude and slowly refills as the solar wind plasma convects downstream. Small perturbations in the magnetic field magnitude are seen downstream of the Moon driven by complex current systems that form around the lunar plasma wake (e.g., Fatemi et al. 2013; Poppe et al. 2014). Generally speaking, the results for the unmagnetized Moon agree well with previous hybrid simulations of the lunar wake in the solar

wind (e.g., Kallio 2005; Wang et al. 2011; Holmström et al. 2012; Vernisse et al. 2013).

As we turn on and increase the strength of the global lunar paleomagnetosphere, the solar wind interaction begins to significantly change. In Figures 3(b) and 4(b), where the uncompressed paleomagnetic field strength at the lunar surface is set to 62.5 nT, the solar wind pressure is high enough to compress the paleomagnetic fields down to the lunar surface, which is consistent with an estimate of the minimum field strength of ~ 100 nT required to stand off the solar wind at 2 Ga (see Equation (1) of Garrick-Bethell et al. 2019). The solar wind does not form a bow shock upstream of the Moon, but compressive wings flaring away and downstream from the Moon are present in both the density and magnetic field magnitude. This case shares some similarities with previous hybrid simulations of potentially magnetized asteroids in the solar wind, where weak perturbations to the interplanetary magnetic field downstream of the asteroids Gaspra and Ida were considered as possible evidence of bulk magnetization (e.g., Kivelson et al. 1995; Omidi et al. 2002; Blanco-Cano et al. 2003; Simon et al. 2006).

In Figures 3(c) and 4(c) and 3(d) and 4(d), where the uncompressed paleomagnetic field strength is set to 125 and 250 nT, respectively, the hallmarks of typical global magnetospheric interactions become apparent. These features include a bow shock upstream of the Moon, dense and heated plasma diverted around and away from the magnetic obstacle along the magnetosheath, and the formation of a pair of low-density magnetotail lobe regions separated by a thin current sheet. In the 125 nT case, Figures 3(c) and 4(c), the magnetopause and bow shock are approximately 0.25 and 0.75 R_L above the surface, respectively. Meanwhile, in the 250 nT case,

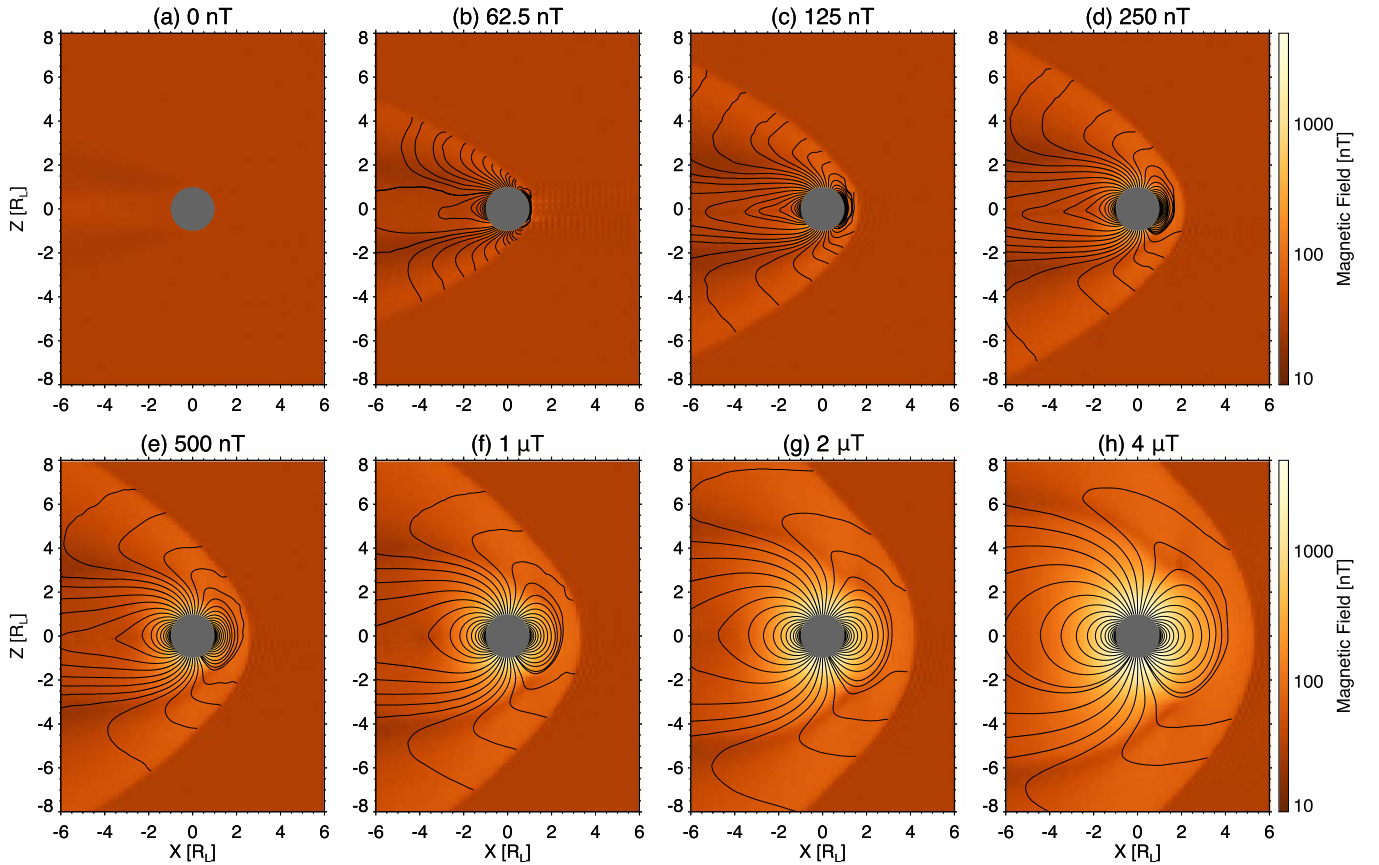


Figure 4. Magnetic field strength in the x - z plane for all eight paleomagnetic field strengths. Field lines are terminated at the bow shock, as the IMF is into the page.

Figures 3(d) and 4(d), the respective magnetopause and bow shock distances are 1.5 and $2.25 R_L$ above the surface. In the density plot in particular, a plasma void above the dayside lunar surface is clearly apparent, as solar wind plasma is effectively diverted around the magnetic obstacle. Both the 125 and 250 nT cases show penetration of solar wind plasma into the northern and southern cusp regions, similar to observations at Mercury, whose ~ 200 nT equatorial surface field—notwithstanding the asymmetries induced by the northward offset of Mercury’s dipole moment—is most closely equivalent to the 250 nT case shown here (e.g., Winslow et al. 2012, 2014; Raines et al. 2014).

As the paleomagnetic field strength continues to increase to 500 nT, $1 \mu\text{T}$, $2 \mu\text{T}$, and, finally, $4 \mu\text{T}$, Figures 3(e)–(h) and 4(e)–(h), respectively, the general characteristics of the lunar paleomagnetosphere remain the same but simply scale upward in size, as expected. Both the upstream magnetopause and bow shock move sunward as the paleo field strength increases, such that for $4 \mu\text{T}$, the respective upstream distances are approximately 2.5 and $4.25 R_L$ above the lunar surface. Densities in the magnetospheric cusp regions are seen in all cases, with local densities greater than three times the upstream solar wind density within the cusps. Additionally, the 1, 2, and $4 \mu\text{T}$ cases all show the presence of quasi-trapped particle distributions on the lunar nightside in the innermost magnetosphere. The size of this quasi-trapping region and the quasi-trapped particle densities therein clearly increase as a function of the paleomagnetic field strength. As discussed below in greater detail, particles within these quasi-trapped regions are accelerated to energies much higher than typical solar wind energies.

3.2. Minor Ion Interactions with the Lunar Paleomagnetosphere

Having presented the global paleomagnetospheric structure as seen via the proton density, we now turn to the interactions of heavy minor solar wind ions with the lunar paleomagnetosphere. Due to the large number of runs, we present only selected results here for discussion.

As an example, Figure 5 shows the particle density relative to the upstream density for protons and all eight minor ion species in the x - z frame for the $1 \mu\text{T}$ case. The proton density, shown in Figure 5(a), is identical to that in Figure 3(f) and shows a well-developed magnetosphere. The eight minor ion species generally show similar features as the protons but with several important differences. First, as the mass-to-charge ratio increases from Figure 5(b) to Figure 5(i), the density structure at the bow shock and within the magnetosheath region changes notably. For the lightest species, M_1^+ and M_2^+ in Figures 5(b) and (c), a relatively smooth enhancement in the particle densities is seen in the magnetosheath as the minor ions are heated, decelerated, and diverted around the paleomagnetosphere. Beginning with the M_3^+ heavy ion in Figure 5(d) and continuing through M_8^+ in Figure 5(i), however, the minor ion densities within the magnetosheath become increasingly striated downstream of the bow shock as a function of the charge-to-mass ratio (discussed further in the next paragraph). The eight minor ion densities also show enhanced populations of trapped particles in the innermost magnetosphere relative to that seen in the protons. While not shown, these ions tend to enter the inner magnetosphere on the duskward flank followed by trapping and circulation in the dipolar magnetospheric

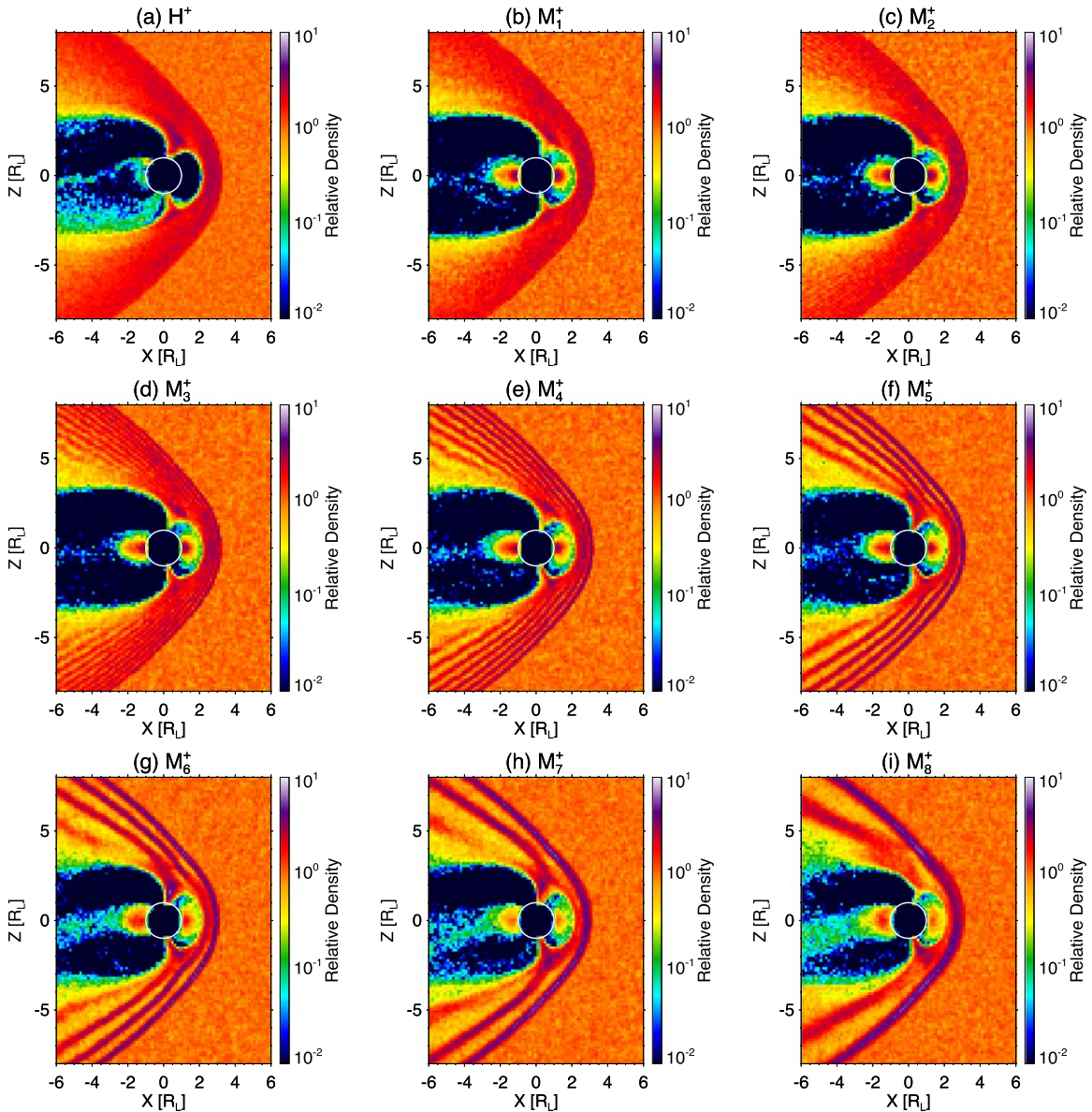


Figure 5. Density relative to the upstream undisturbed density in the x - z plane for all nine ions (protons and eight heavy minor ions) for the $1 \mu\text{T}$ paleomagnetic field strength case.

region. Precipitation to the lunar surface is a major loss term for these trapped ions (as discussed later), while magnetopause shadowing on the dayside also likely plays a role in particle loss from the trapped region (e.g., Sibeck et al. 1987; Klida & Fritz 2009; Sorathia et al. 2017). Finally, all eight heavy ions show varying degrees of precipitation through the northern and southern cusp regions, similar to that seen for protons.

With regard to the striations in the heavy ion density in the magnetosheath, previous observations and one-dimensional hybrid modeling of He^{2+} interactions with the terrestrial bow shock have demonstrated the existence of “ring beam” velocity distributions within the terrestrial magnetosheath, driven by differential deceleration of higher mass-to-charge ions across the cross-shock potential (e.g., Fuselier et al. 1988; Motschmann & Glassmeier 1993; Fuselier & Schmidt 1997; Lu & Wang 2005; Tsubouchi et al. 2016). An alternative way of understanding these structures is to realize that the heavy ions undergo prolate trochoid motion upon crossing the bow shock, where the magnetic field strength, convection velocity, and

convection electric field all abruptly change. Prolate trochoid ion motion is also seen in solar wind protons that reflect from the lunar surface and/or crustal magnetic anomalies and are “re-picked up” by the solar wind (e.g., Nishino et al. 2013; Halekas et al. 2014b, 2017). The increased distance between the striations as a function of the minor ion mass-to-charge ratio reflects the increase in ion gyroradius, which controls the distance at which the ions reach a velocity minimum and associated density maximum. Similar striated features in the minor ion densities are not apparent in the hybrid model results of Kallio et al. (2008; see their Figures 2(b)–(c)); however, the panels in Kallio et al. (2008) are in the equatorial x - y plane, and the corresponding densities in the x - z plane were not presented. Furthermore, the $^{16}\text{O}^{7+}$ ion simulated by Kallio et al. (2008) has a mass-to-charge ratio of approximately 2.3 and would correspond roughly with our M_2^+ in Figure 5(c), where density striations in the magnetosheath are not readily evident in our simulations (most likely due to the spatial grid size being larger than the characteristic gyroscale for $^{16}\text{O}^{7+}$ ions).

The $^{56}\text{Fe}^{9+}$ ion possesses a mass-to-charge ratio of 6.2 and most closely matches M_5^+ in Figure 5(f), where striations are clearly seen in our simulations. Simulation results from both Shimazu (2001), who studied solar wind interactions with unmagnetized planets with dense ionospheres, and Simon et al. (2006), who studied the solar wind interaction with magnetized asteroids, show similar striated density features along with sample solar wind proton trajectories demonstrating the same prolate trochoid motion (see, in particular, Figure 6 of Shimazu 2001 or Figure 5 of Simon et al. 2006).

3.3. Minor Ion Precipitation to the Lunar Surface

3.3.1. Spatial Precipitation Maps

In addition to mapping the spatial structure of proton and minor ion densities within the lunar paleomagnetosphere, the Amitis hybrid model also tracks the precipitation of ions to the surface of the Moon. For each combination of paleomagnetic field strength and ion mass, we constructed ion precipitation flux maps spatially resolved onto the lunar surface in $5^\circ \times 5^\circ$ longitude and latitude bins by aggregating the macroparticles incident at each location, multiplying by the macroparticle weight, and dividing by the local surface area. Figures 6(a)–(i) show the precipitation flux map for all nine ion species for the control case with no paleomagnetic field (i.e., $B = 0$ nT), with each panel normalized to the mean precipitation flux at the subsolar point. With no paleomagnetic field, all solar wind ions precipitate directly onto the sunward lunar hemisphere. Finite ion temperatures cause some extension of the precipitating ion flux past the terminators (i.e., subsolar longitudes equal to $\pm 90^\circ$). For solar wind protons, seen in Figure 6(a), the deep nightside surface is free of any precipitation past solar zenith angles of approximately 120° , as the solar wind proton thermal gyroradius of ≈ 20 km prevents any deep nightside access. For the minor ions, however, small precipitating fluxes on the order of 10^{-3} – 10^{-2} times the subsolar precipitating flux are apparent on the deep nightside lunar surface. Despite this small feature, we emphasize that the dominant region of precipitation for the unmagnetized Moon is on the lunar dayside.

In comparison, Figures 6(j)–(r) show the relative surface precipitation fluxes for all nine ion species for the $1 \mu\text{T}$ paleomagnetic field case (i.e., the same case as that shown in Figure 5). Here one can see that the precipitation patterns are drastically altered by the presence of the paleomagnetic fields in comparison to the unmagnetized case. For protons, Figure 6(j), precipitating fluxes are completely shielded for nearly the entire lunar dayside. Peak precipitating fluxes occur along a narrow strip in the southern polar region between subsolar longitudes of -180° to $+30^\circ$, along a narrow strip in the northern hemisphere at latitudes of approximately $+60^\circ$ between longitudes of 90° and 180° , and, finally, in a roughly circular region in the southern hemisphere centered at approximately -30° latitude and 150° longitude. The first of these regions (i.e., the narrow strip near the southern pole) is due to precipitation of protons through the southern magnetic cusp region, as can be seen in the density in Figure 5(a). The corresponding region of precipitation in the northern hemisphere is much weaker, most likely due to asymmetries induced by the sense of the convection electric field, which points in the $+\hat{z}$ direction and thus drives more precipitation into the southern hemisphere than in the north. The two latter regions of precipitation at lower respective latitudes are due to the

precipitation of quasi-trapped protons in the inner magnetosphere (also visible on the lunar nightside in Figure 5(a)). For protons, the trapped regions are not particularly well populated (at least compared to the heavier minor ions); thus, the precipitation via inner magnetospheric trapping, while present, is not overly dominant.

In contrast to the proton precipitation map in Figure 6(j), the precipitation maps for heavier minor ions shown in Figures 6(k)–(r) are markedly different. Generally speaking, for the eight minor ion species, two regions of precipitation are present in varying strengths: (1) a pair of localized conjugate regions at high latitudes ($> \approx 70^\circ$) in both the northern and southern hemispheres near the subsolar meridian and (2) a narrow equatorial band wrapping around nearly the entire lunar circumference. The localized regions of precipitation near the northern and southern poles correspond to precipitation through the dayside cusp regions of the lunar paleomagnetosphere. The magnitude of this precipitating flux increases by approximately 1 order of magnitude from the lightest minor ion, M_1^+ in Figure 6(l), to the heaviest minor ion, M_8^+ in Figure 6(r). The corresponding density structures of ions being focused into the cusp regions and down to the lunar surface can be clearly seen in the density plots, Figures 5(b)–(i). The second main region of precipitation, namely, the narrow band centered on the equator for all minor ions, is a result of precipitation from quasi-trapped particles in the innermost paleomagnetosphere. The precipitation in this region is highest for the lightest minor ion, M_1^+ in Figure 6(k), with relative fluxes greater than a factor of 10 over the unmagnetized case, Figure 6(b). As the mass-to-charge ratio increases, the relative magnitude of the equatorial precipitation region decreases, such that for the heaviest minor ion, Figure 6(r), the equatorial region precipitation is on the order of 0.1 times the corresponding unmagnetized flux at the subsolar point. Additionally, the equatorial precipitation region increases in latitudinal thickness as the minor ion mass-to-charge ratio increases, and, for the heaviest minor ions, M_6^+ , M_7^+ , and M_8^+ in Figures 6(p), (q), and (r), respectively, a pair of narrow lines of precipitation appears on the lunar nightside at latitudes of $\pm 30^\circ$ – $\pm 60^\circ$. These regions represent precipitation by particles at their high-latitude mirror points within the trapped inner magnetospheric region.

3.3.2. Precipitation Energy Distributions

In addition to the spatial distribution of ion precipitation to the lunar surface, the Amitis hybrid model also tracks the velocity, and thus energy, at which ions strike the lunar surface. Figure 7 shows the distribution of ion impact energies integrated over the entire surface for all eight cases of the paleomagnetic field strength. Figure 7(a) shows the control case with no paleomagnetic fields (0 nT). Here all ions, regardless of charge-to-mass ratio, impact the lunar surface at respective energies corresponding to the solar wind drift speed of 550 km s^{-1} . Impact energies range from ~ 1 keV for the lightest ion (i.e., protons) to ~ 200 keV for the heaviest simulated ion, M_8^+ . The increase in impact energy seen as a function of q/m is simply the mass scaling, since the impact velocity in this case remains constant, i.e., $E_{\text{imp}} = 0.5 m_i v_{\text{sw}}^2$. The impact energy distributions for each individual ion in this case are also very narrow, corresponding to the relatively cold temperature of solar wind ions.

As the paleomagnetic field strength increases, the impact energy distributions change as the incident solar wind ions interact with the paleomagnetic fields before striking the

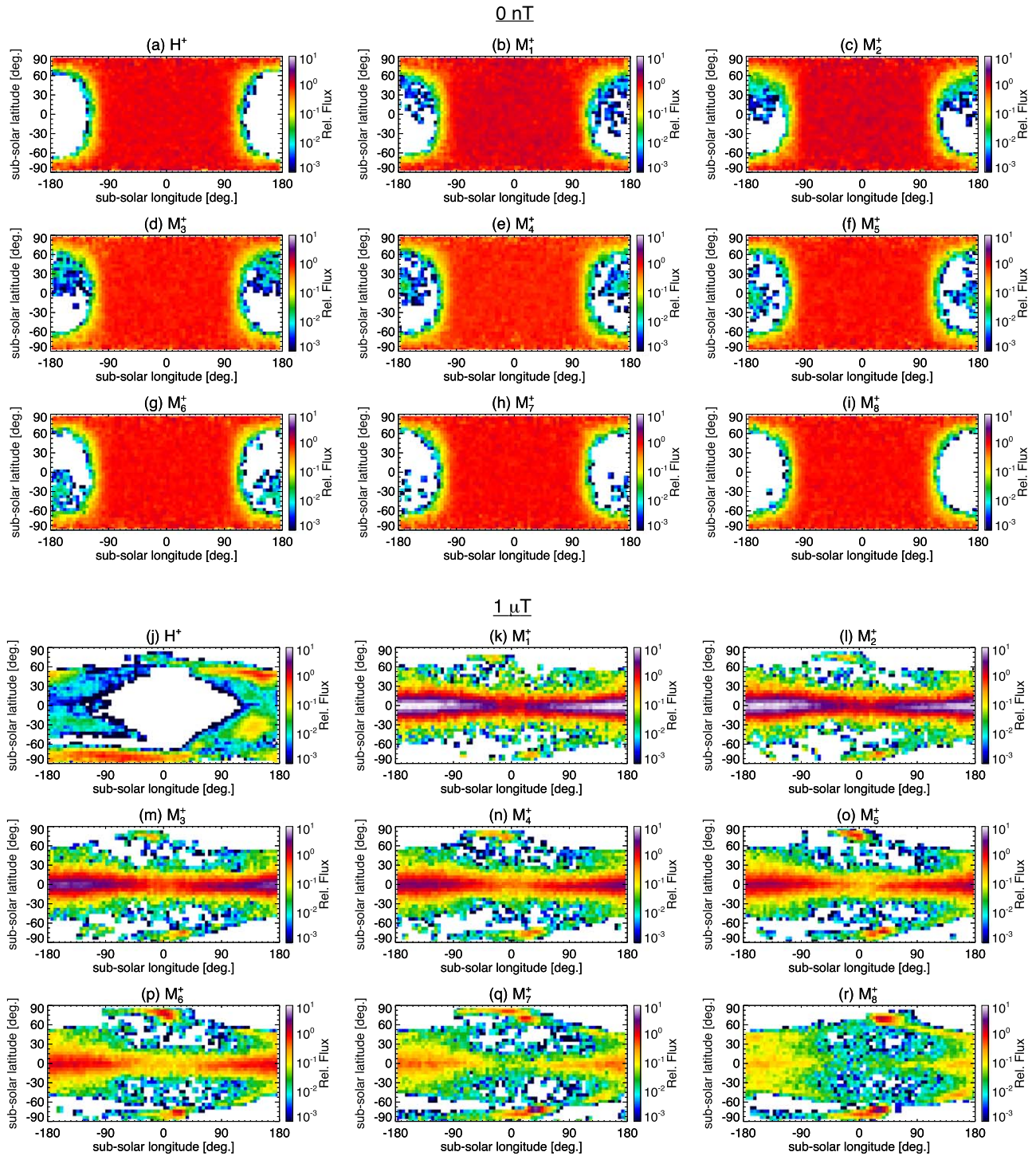


Figure 6. Surface precipitation maps for protons and all eight heavy ions for (a)–(i) the 0 nT case and (j)–(r) the 1 μ T case. Maps for each individual ion are normalized to the subsolar flux in the 0 nT case.

surface. These interactions can either decrease or increase the ion impact energies relative to the distributions in the 0 nT case. For the two lowest paleomagnetic field strengths of 62.5 nT and 125 nT, the ion impact energies shown in Figures 7(b) and (c), respectively, share the same general trend as the 0 nT case, namely, an overall increase in ion impact energy that scales as the ion mass. In addition to this trend, however, the ion impact energies in these two cases have extended “tails” to lower impact energies, demonstrating that weak paleomagnetic fields can slightly decelerate solar wind ions of all masses before they

strike the lunar surface. Starting with the 125 nT paleomagnetic fields, Figure 7(c), and continuing to stronger paleomagnetic field strengths, the energy distribution for the protons begins to decrease in energy, while the energy distributions for the heavy ions begin to have tails that extend to higher energies. As field strengths increase to 250 nT, 500 nT, and 1 μ T, Figures 7(d), (e), and (f), respectively, the bulk impact energies of the heavy ions increase significantly as well. Indeed, for the 1 μ T case, the heavy ion energy distributions reach maxima on the order of 1 MeV ($\equiv 10^6$ eV). Finally, for the 2 and 4 μ T cases,

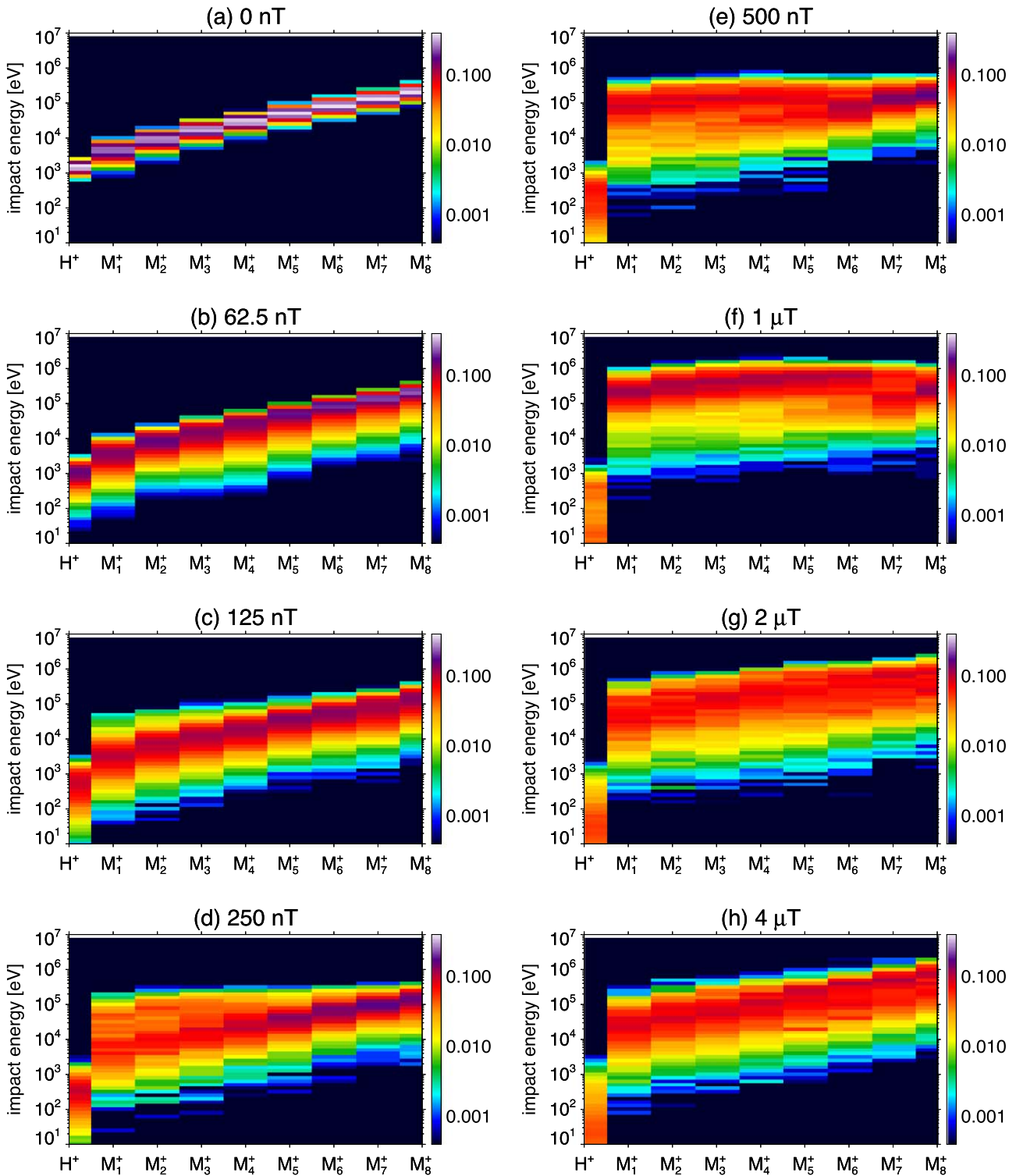


Figure 7. Impact energy distributions for the protons and all eight heavy minor ions for all eight paleomagnetic field cases (including the 0 nT control case). The energy distributions for each individual ion are normalized such that the integral of the distribution over energy is unity.

Figures 7(g) and (h), respectively, the energy distributions for the heavy ions decrease slightly compared to the 1 μT case but still remain elevated compared to the 0 nT case in Figure 7(a).

3.3.3. Relative Precipitation Fluence

Finally, we have calculated the total precipitation fluence to the lunar surface for each ion species and paleomagnetic field

strength. To do so, we first integrated the spatially resolved flux to the lunar surface (i.e., Figure 6) over area. Using the fluences calculated for the 0 nT “control” case, we then normalized the fluences for each ion in the cases with paleomagnetic fields to the fluences calculated for the 0 nT case. The “relative fluence” thus quantifies the degree to which paleomagnetic fields either suppress or enhance the total delivery of ions to the lunar surface and is shown in Figure 8. For the 62.5 nT case,

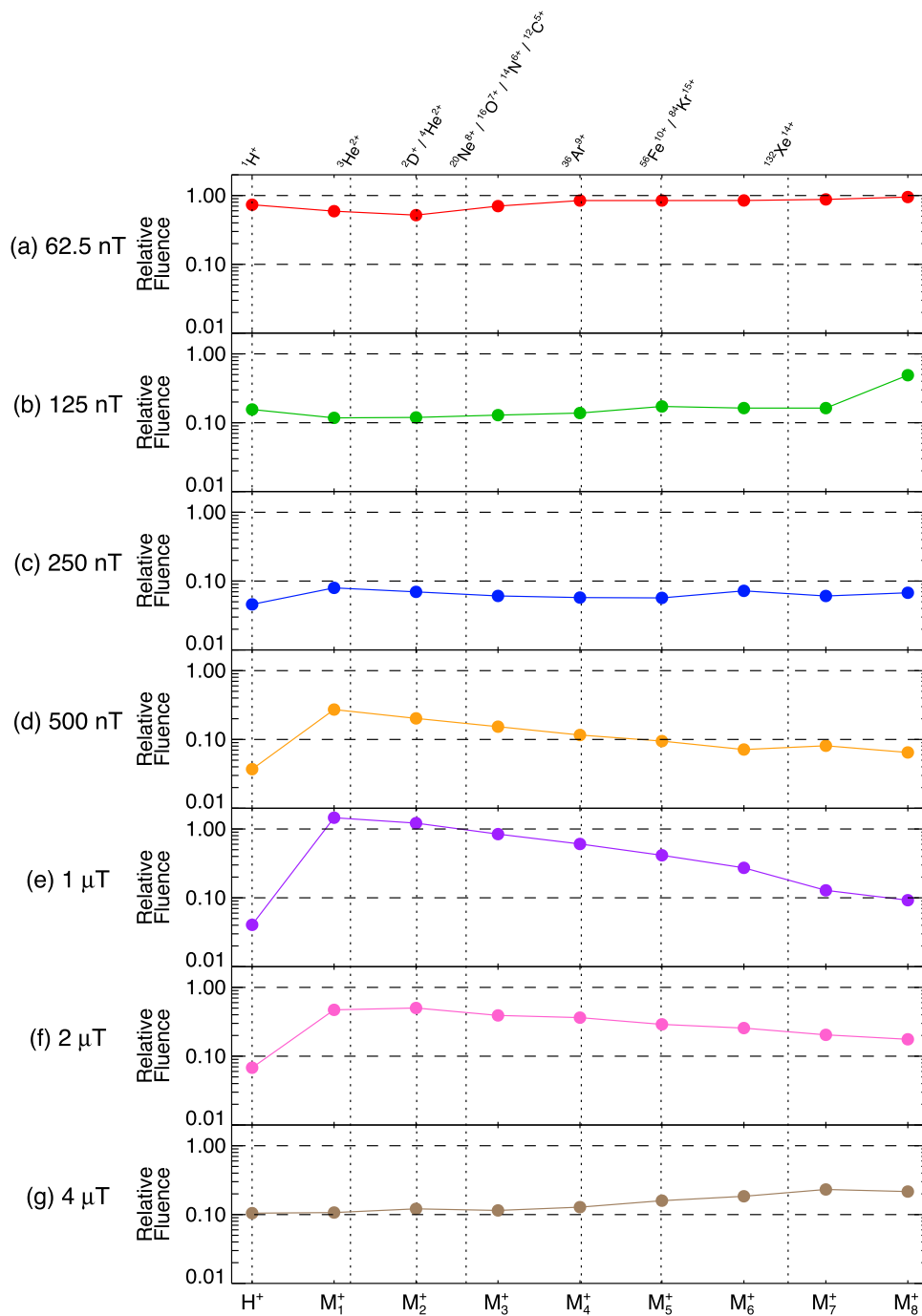


Figure 8. Relative precipitating fluence for all eight heavy minor ions (M_1^+ to M_8^+) for the seven nonzero paleomagnetic field cases. The vertical dotted lines denote the charge-to-mass ratios for specific solar wind minor ions, as denoted at the top of the figure.

Figure 8(a) in red, relative fluences for all ions are slightly depressed, with the largest decrease occurring for minor ion M_2^+ . For ions with the lowest charge-to-mass ratios, such as M_6^+ , M_7^+ , and M_8^+ , the suppression of fluence is very small, with a relative fluence near ~ 0.95 . For the 125 and 250 nT cases, shown in Figures 8(b) in green and 8(c) in blue, the relative fluences for nearly all ions are strongly suppressed. For 125 nT, the relative fluences have a mean value of ~ 0.15 (excluding the heaviest ion, M_8^+ , which has a relative fluence near 0.5), indicating that the paleomagnetic fields have blocked nearly 85% of the solar wind fluence to the surface. For 250 nT, the suppression is even greater (and, in fact, is the

paleomagnetic field case with the lowest relative fluence averaged over all ion species) with a mean relative fluence of ~ 0.06 , now including M_8^+ as well.

Starting with the 500 nT case, shown in Figure 8(d) in yellow, a new pattern emerges. Here the relative fluence for protons, H^+ , continues to decrease slightly, while the relative fluences for the minor ions begin to increase. For example, the relative fluence for the lightest minor ion, M_1^+ , jumps to ~ 0.25 , a value higher than both the 250 and 125 nT cases. This trend continues for the 1 μ T case, Figure 8(e) in purple, where the proton relative fluence remains very low (~ 0.04), while the relative fluences for the minor ions have increased such that

those for M_1^+ and M_2^+ (near ${}^3\text{He}^{2+}$ and ${}^4\text{He}^{2+}$, respectively) are in fact above 1.00, meaning that the paleomagnetic fields have actually increased their fluence to the surface relative to the unmagnetized case. Finally, for the two strongest paleomagnetic field cases, 2 μT shown in Figure 8(f) in pink and 4 μT shown in Figure 8(g) in brown, the enhancement trend in the relative fluence declines again, with peak relative fluences for the 2 and 4 μT cases of 0.50 and 0.23, respectively.

4. Discussion

As demonstrated above, the interaction of solar wind protons and heavy minor ions with lunar paleomagnetospheric fields is complex and does not admit simple linear scaling laws (i.e., a statement such as “stronger paleomagnetic fields yield lower heavy ion flux” does not hold). Here we discuss the underlying mechanisms that govern the complex “magnetospheric fractionation” patterns seen in the model results. We also discuss the implications of these results for the interpretation of both solar wind material implanted in lunar soil and the use of the ${}^{40}\text{Ar}/{}^{36}\text{Ar}$ antiquity indicator. Before doing so, we wish to reemphasize that the study results presented above and the conclusions discussed below are based on a necessarily incomplete picture of the full lunar paleomagnetic/solar wind interaction. As discussed in Section 2.1, our simulations have focused primarily on only two variables: (i) the solar wind ion mass-to-charge ratio and (ii) the strength of the lunar paleomagnetic fields. Many additional variables, including—but certainly not limited to—variations in the upstream solar wind and IMF parameters (e.g., density, velocity, alpha fraction, IMF orientation), the orientation of the lunar paleodipole and the presence of higher-order magnetic moments (and any time variability that may be present in these values), and the role that the terrestrial magnetosphere may play (e.g., especially as the Moon transits the terrestrial magnetosheath, which consists of shocked and diverted solar wind plasma), are certain to play important roles. All of these variables are noted as rich areas for future research. Keeping these limitations in mind, we proceed to discuss various implications derived from our current set of simulations.

The various patterns in the precipitation energy distributions, Figure 7, across both paleomagnetic field strength and ion charge-to-mass can be related back to patterns seen in both the spatial density distributions seen in Figure 5 and spatial precipitation maps seen in Figure 6. In the presence of paleomagnetic fields, protons are generally able to access the lunar surface through the magnetospheric cusp regions with much smaller contributions on the lunar nightside from the quasi-trapped inner magnetosphere region. Protons appear far less able to penetrate into the closed field region of the inner paleomagnetosphere and precipitate to the surface, potentially due to their role as the dominant charge and current carriers in the simulations (as opposed to the heavy ions, which act only as “test particles”). In contrast to the protons, the characteristics of the heavy ion precipitation energy distribution are strongly governed by their dynamics with the quasi-trapped region in the inner magnetosphere. As the charge-to-mass ratio increases, the ion gyroradii correspondingly increase. In turn, larger ion gyroradii increase the probability of nonadiabatic ion motion, when the first adiabatic moment of a particle is not conserved. Among other effects, nonadiabatic motion can lead to both ion access onto closed field lines, where ions subsequently populate the inner paleomagnetospheric region, and ion

energization, as ions interact with small-scale electric fields with typical sizes less than the corresponding ion gyroradius, which then yield a net energy gain (e.g., Massetti et al. 2007; Zelenyi et al. 2007; Keika et al. 2013; Walker et al. 2013). These energized heavy minor ions then continuously precipitate to the lunar surface at energies up to 1 MeV as their relatively large gyroradii allow them direct access to the lunar surface.

The relative ion fluence to the lunar surface seen in Figure 8 also reflects various aspects of the solar wind interaction with the lunar paleomagnetosphere. For the three lowest paleomagnetic field strengths, 62.5, 125, and 250 nT, the dominant trend is the overall suppression of ion fluence to the lunar surface with only slight fractionation as a function of ion charge-to-mass ratio (recall that charge-to-mass ratio decreases from H^+ to M_7^+ ; see Table 1). Paleo fields of this magnitude are able to shield the lunar surface by over 90% (in terms of fluence) by simple deflection of the solar wind around the magnetic obstacle. In particular, when summed over all ions, the 250 nT case is the most effective at shielding the lunar surface from solar wind ion fluence. We do note that for weaker paleomagnetic field strengths (62.5 and 125 nT), the highest m/q ions (e.g., M_7^+ and M_8^+) have gyroradii generally large enough to fully transit through the relatively weak bow shock and precipitate directly to the surface. This emphasizes the highly kinetic nature of the solar wind minor ion interaction with the lunar paleomagnetosphere.

Once the field strengths reach 500 nT and greater, however, a more robust magnetospheric structure begins to emerge and with it, more efficient funneling of solar wind plasma through the high-latitude cusps and more densely populated trapped particle regions. These two effects (cusp precipitation and trapped particle precipitation) more strongly fractionate the ion fluence as a function of ion charge-to-mass ratio. In particular, as seen in Figure 8(e) for 1 μT fields, the ratio of $\text{M}_1^+/\text{M}_8^+$ fluences to the lunar surface is on the order of ~ 15 . Furthermore, when taken over all minor ions, the 1 μT case has the second-highest fluence to the lunar surface (second only to the 62.5 nT case, where ions can still readily access the lunar dayside). Finally, for field strengths of 2 and 4 μT , the decline in the surface fluence with respect to the 1 μT case represents the combined effects of a decrease in the efficiency of funneling solar wind ions through the magnetospheric cusps and outward expansion of the trapped particle region that reduces the likelihood of quasi-trapped particles striking the surface. Both of these changes are simply due to increased magnetic field strengths; e.g., stronger fields lead to both more efficient magnetic mirroring of ions in the magnetospheric cusps before they can impact the surface and smaller ion gyroradii in the innermost quasi-trapped regions, which also decreases the likelihood of ion precipitation.

Given the complex and significant impacts that the lunar paleomagnetosphere has on the incident solar wind, as discussed above, we conclude that paleomagnetic fields have strong implications for the interpretation of implanted solar wind species in the lunar regolith, especially for lunar soil grains that are from the paleomagnetic epoch, roughly 4.5–1.0 Gya (Weiss & Tikoo 2014; Tikoo et al. 2017; Mighani et al. 2020). If we take our 4 μT case as indicative of the low-field paleomagnetic epoch (3.5–1.0 Ga), then the presence of the lunar paleomagnetosphere may have fractionated the solar wind minor ion population as a function of charge-to-mass ratio by approximately a factor of 2 between protons and Xe ions

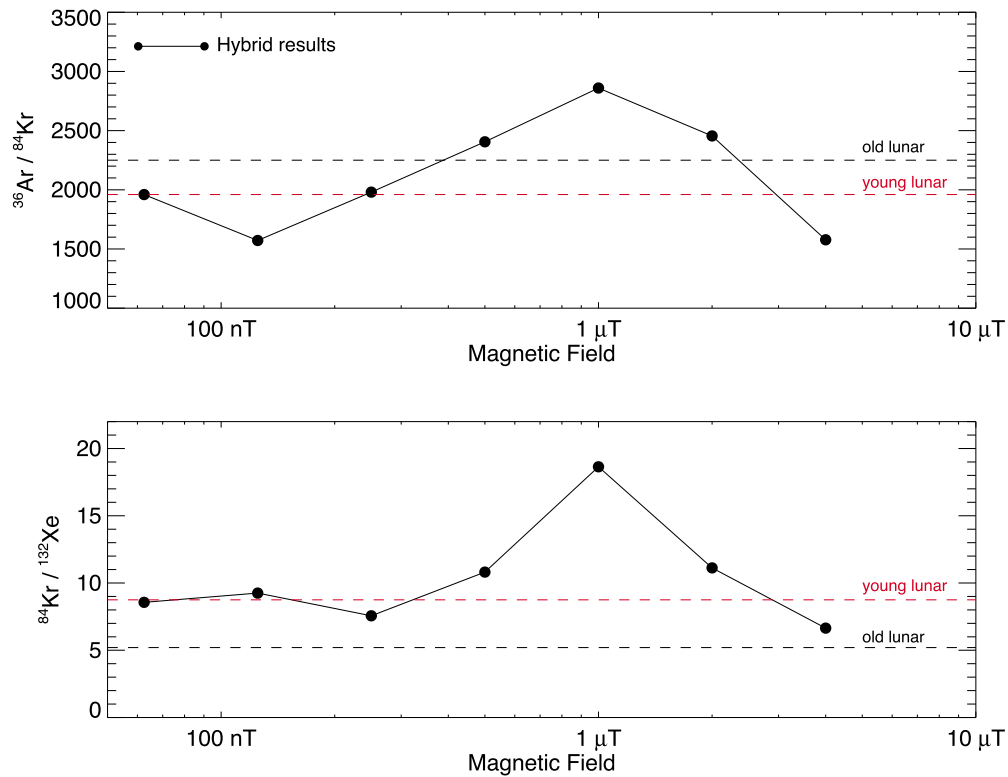


Figure 9. Fractionation predicted by the hybrid results as a function of paleomagnetic field strength for (top) $^{36}\text{Ar}/^{84}\text{Kr}$ and (bottom) $^{84}\text{Kr}/^{132}\text{Xe}$ relative to the isotopic ratio determined from “young” lunar samples (red dashed lines). The respective isotopic ratios for “old” lunar samples are shown as the black dashed lines.

(which lies roughly between our synthetic M_6^+ and M_7^+ ions). Such fractionation could be partially responsible for secular trends observed in either the Ar/Kr or Kr/Xe ratio (or both) between high- and low-antiquity samples, as shown in Figure 1 (e.g., Becker & Pepin 1989; Wieler & Baur 1995; Wieler et al. 1996; Wieler 2016). As an example, Figure 9 shows the hybrid model predictions for the isotopic ratios of precipitating ions of $^{36}\text{Ar}/^{84}\text{Kr}$ and $^{84}\text{Kr}/^{132}\text{Xe}$ as a function of the paleomagnetic surface field strength, normalized such that our 0 nT case matches the “young” lunar isotopic ratios reported in Wieler (2016) and shown here in Figure 1. Both ratios show strong negative and positive deviations with respect to the observed “young” lunar isotopic ratios. For the $^{36}\text{Ar}/^{84}\text{Kr}$ ratio, the predicted isotopic deviations from the hybrid model wholly encompass the deviation seen between “young” and “old” lunar samples (red and black dashed lines, respectively). For $^{84}\text{Kr}/^{132}\text{Xe}$, the negative isotopic ratio deviation seen in the “old” lunar samples is nearly matched by the hybrid model for the 4 μT case. Intriguingly, the trend in the modeled $^{84}\text{Kr}/^{132}\text{Xe}$ seen in 1, 2, and 4 μT suggests that paleomagnetic field strengths of $\sim 6\text{--}8 \mu\text{T}$ may yield a closer match to the observed ratio in “old” lunar samples. We do note that the predicted isotopic ratios from the hybrid model do not appear to simultaneously match both the $^{36}\text{Ar}/^{84}\text{Kr}$ and $^{84}\text{Kr}/^{132}\text{Xe}$ ratios for a specific paleomagnetic field strength.

Our simulation results also have implications for the use of the $^{40}\text{Ar}/^{36}\text{Ar}$ ratio in lunar grains as a standard semiquantitative antiquity indicator (e.g., Eugster et al. 2001; Joy et al. 2011). As discussed in, e.g., Joy et al. (2011), the $^{40}\text{Ar}/^{36}\text{Ar}$ antiquity indicator operates by assuming that (i) the flux of solar wind ^{36}Ar to the lunar surface remains constant over geologic time and (ii) the flux of ionized ^{40}Ar to lunar soil scales in time as the abundance of its radiogenic parent, ^{40}K , with a half-life of

~ 1.25 Gyr. Neither of these assumptions may hold, however. For the former assumption, we first note that the solar wind flux is believed to have decreased by nearly 2 orders of magnitude over its lifetime (e.g., Wood et al. 2005; Airapetian & Usmanov 2016); thus, even the undisturbed flux of ^{36}Ar to the Moon may have a strong time dependence. Second, as noted by Tikoo et al. (2017) in their analysis of the antiquity of Apollo sample 15498, the $^{40}\text{Ar}/^{36}\text{Ar}$ antiquity indicator may be subject to increased uncertainty due to the presumed shielding ability of solar wind ^{36}Ar by lunar paleomagnetic fields. Our simulations confirm this point that the presence of the lunar paleomagnetosphere may have significantly altered the incident solar wind flux of ^{36}Ar to the lunar surface (note that $^{36}\text{Ar}^{9+}$ has a charge-to-mass ratio nearly identical to our synthetic heavy ion, M_4^+). The overall relative fluence of M_4^+ ions to the lunar surface in the presence of a 4 μT lunar paleomagnetic field is on the order of 0.1 but highly spatially inhomogeneous. For the latter assumption, the presence of the lunar paleomagnetosphere is also likely to alter the reimplantation flux of native ^{40}Ar ions to the lunar surface from the commonly cited Manka & Michel (1970)–type recycling. While we have not yet addressed the paleomagnetospheric effects on $^{40}\text{Ar}^+$ ion circulation, we can expect a wealth of complex dynamics simply by analogy to previous observations and modeling of planetary ions at Mercury (e.g., Yagi et al. 2010, 2017; Zurbuchen et al. 2011; Raines et al. 2013, 2014, 2015; Seki et al. 2013; Walsh et al. 2013; Aizawa et al. 2017).

At this point, we hesitate to conjecture too wildly, but some questions regarding the interpretation of the $^{40}\text{Ar}/^{36}\text{Ar}$ antiquity indicator do present themselves. Does the observed empirical decrease of the $^{40}\text{Ar}/^{36}\text{Ar}$ ratio in lunar samples as a function of time (where high-antiquity samples near 4.0 Ga have ratios of ~ 15 , and current-day samples have ratios < 1 ; e.g., Figure 4 of Eugster et al. 2001 or Figure 2 of Joy et al. 2011)

reflect both the known radioactive decay of ^{40}K , which decreases the available ^{40}Ar as a function of time, and an increase in solar wind ^{36}Ar fluence to the lunar surface due to the declining paleomagnetic field strength? If the answer is “yes,” then does this imply that less ^{40}K was primordially present in the lunar crust than currently assumed? Or does a decrease in the flux of lunar ^{40}Ar ions from the lunar atmosphere imply lower effusion rates of ^{40}Ar from the lunar crust and interior or changes in the assumed abundance and depth distribution of ^{40}K (e.g., Killen 2002)? On the other hand, for earlier geologic epochs, is the paleomagnetic-related decrease in the relative fluence of solar wind ^{36}Ar to the lunar surface actually counterbalanced by the increased solar wind flux at the Moon, which has changed by almost 2 orders of magnitude over the Sun’s lifetime (e.g., Wood et al. 2005; Airapetian & Usmanov 2016; Ó Fionnagáin & Vidotto 2018; Carolan et al. 2019)? The answer to these questions lies in further modeling and analysis of solar wind interactions with lunar paleomagnetic fields over a wider range of both upstream solar wind and paleomagnetic field parameters. Additionally, the dynamics of ionized lunar ^{40}Ar ions within lunar paleomagnetospheres of varying magnitude are clearly needed in order to understand how such fields may have altered the recycling of lunar ^{40}Ar ions (e.g., as highlighted by Tikoo et al. 2017), as the Manka & Michel (1970)–type recycling of atmospheric ions by the undisturbed solar wind convection electric field does not apply in the presence of paleomagnetic fields.

5. Conclusion




Using the three-dimensional Amitis hybrid plasma model, we have simulated the interaction of solar wind protons and heavy minor ions with the lunar paleomagnetosphere over a range of assumed paleomagnetic field strengths. The hybrid model results show the successive growth of a lunar paleomagnetosphere with increasing surface magnetic field strength, in line with previous hybrid simulations performed by Garrick-Bethell et al. (2019). Simultaneous modeling of the dynamics of heavy minor solar wind ions with the lunar paleomagnetosphere have demonstrated that the fluence of these ions to the lunar surface is heavily altered by the presence of paleomagnetic fields. While solar wind ions of all charge-to-mass ratios impact the dayside lunar surface directly for an unmagnetized Moon, the presence of a paleomagnetic field shields the dayside lunar surface by up to an order of magnitude in fluence. Despite this dayside shielding effect, precipitation of solar wind minor ions through the paleomagnetospheric cusps and from trapped ions in the inner magnetospheric dipolar region still allows solar wind minor ions to reach the lunar surface. In most of the cases we studied, paleomagnetospheric fields suppressed the overall fluence of minor ions relative to the unmagnetized case; however, in two particular cases (the M_1^+ and M_2^+ synthetic heavy ions with 1 μT paleomagnetic fields), the paleomagnetospheric fields actually increased the relative fluence of solar wind minor ions to the lunar surface due to highly efficient trapping and subsequent precipitation of ions in the inner dipolar magnetospheric region. In addition to altering the net fluence of minor ions to the lunar surface, interactions with the lunar paleomagnetosphere also significantly increased the energies at which solar wind minor ions impact the surface. For paleomagnetospheric field strengths typical of that estimated

for the low-field epoch, e.g., $5 \pm 2 \mu\text{T}$ (Tikoo et al. 2017), ion impact energies increase up to 1 MeV, an order of magnitude or more greater than their impact energies for the unmagnetized case.

Overall, the simulation results have extensive implications for the interpretation of implanted solar wind species in lunar regolith and, in reality, make an already difficult interpretation all the more challenging. Nevertheless, based on our findings presented here, we maintain that the presence of lunar paleomagnetic fields—which are now well documented in the literature (e.g., Shea et al. 2012; Weiss & Tikoo 2014; Tikoo et al. 2014, 2017)—and their subsequent effects must be accounted for in studies of moderate-to-high-antiquity lunar samples. Further exploration of the nature of magnetospheric fractionation is also clearly warranted, including, for example, studies of the effects of varying solar wind conditions, paleomagnetic dipole orientations, and the possible presence of higher-order magnetic moments on the precipitation of solar wind minor ions. Consideration of the impact of the lunar paleomagnetosphere on the precipitation of terrestrial plasma to the lunar surface is also a future avenue for exploration (e.g., Ozima et al. 2005; Terada et al. 2017; Green et al. 2020). Additionally, further constraints on the magnitude and timing of lunar paleomagnetic fields will help to inform the relationship between the exposure age of a sample and the magnetospheric environment in which a given sample acquired any exogenous implanted material.

A.R.P. and I.G.-B. acknowledge support through NASA’s Solar System Workings program, grant No. 80NSSC19K0560. S.F. acknowledges support from the Swedish National Space Agency, grant No. 179/18. The authors also acknowledge constructive reviews from two anonymous reviewers.

ORCID iDs

A. R. Poppe  <https://orcid.org/0000-0001-8137-8176>
I. Garrick-Bethell  <https://orcid.org/0000-0002-6327-5867>
S. Fatemi  <https://orcid.org/0000-0002-9450-6672>

References

- Aellig, M. R., Lazarus, A. J., & Steinberg, J. T. 2001, *GeoRL*, **28**, 2767
Airapetian, V. S., & Usmanov, A. V. 2016, *ApJL*, **817**, L24
Aizawa, S., Delcourt, D., & Terada, N. 2017, *GeoRL*, **45**, 595
Anderson, B. J., Johnson, C. L., Korth, H., et al. 2011, *Sci*, **333**, 1859
Baek, S.-M., Kim, K.-H., Garrick-Bethell, I., & Jin, H. 2019, *JGRE*, **124**, 223
Becker, R. H., & Clayton, R. N. 1975, *LPSC*, **6**, 2131
Becker, R. H., & Pepin, R. O. 1989, *GeCoA*, **53**, 1135
Becker, R. H., & Pepin, R. O. 1994, *Metic*, **29**, 724
Benkert, J.-P., Baur, H., Signer, P., & Wieler, R. 1993, *JGR*, **98**, 13147
Blanco-Cano, X., Omid, N., & Russell, C. T. 2003, *JGRA*, **108**, 1216
Bochsler, P. 1987, *PhyS*, **T18**, 55
Bochsler, P. 2000, *RvGeo*, **38**, 247
Bochsler, P. 2007, *A&ARv*, **14**, 1
Bochsler, P., Fludra, A., & Giunta, A. 2017, *SoPh*, **292**, 128
Carolan, S., Vidotto, A. A., Loesch, C., & Coogan, P. 2019, *MNRAS*, **489**, 5784
Cisowski, S. M., Collinson, D. W., Runcorn, S. K., Stephenson, A., & Fuller, M. 1983, *JGR*, **88**, A691
Crowther, S. A., & Gilmour, J. D. 2013, *GeCoA*, **123**, 17
Dmitriev, A. V., Suvorova, A. V., & Veselovsky, I. S. 2011, in *Handbook on Solar Wind: Effects, Dynamics, and Interactions*, Vol. 81, ed. H. E. Johannson (New York, NY: NOVA Science Publishers)
Eugster, O., Eberhardt, P., & Geiss, J. 1969, *JGR*, **74**, 3874
Eugster, O., Terribilini, D., Polnau, E., & Kramers, J. 2001, *M&PS*, **36**, 1097
Fagan, A. L., Joy, K. H., Bogard, D. D., & Kring, D. A. 2014, *EM&P*, **112**, 59
Fatemi, S., Holmström, M., Futaana, Y., et al. 2014, *JGRA*, **119**, 6095

- Fatemi, S., Holmström, M., Futaana, Y., Barabash, S., & Lue, C. 2013, *GeoRL*, **40**, 17
- Fatemi, S., Poppe, A. R., & Barabash, S. 2020, *JGRA*, **125**, e27706
- Fatemi, S., Poppe, A. R., Delory, G. T., & Farrell, W. M. 2017, *J. Phys.: Conf. Series*, 837
- Fuqua Haviland, H., Poppe, A. R., Fatemi, S., Delory, G. T., & de Pater, I. 2019, *GeoRL*, **46**, 4151
- Füri, E., Zimmerman, L., Deloule, E., & Trappitsch, R. 2020, *E&PSL*, **550**, 116550
- Fuselier, S. A., & Schmidt, W. K. H. 1997, *JGR*, **102**, 11273
- Fuselier, S. A., Shelley, E. G., & Klumpar, D. M. 1988, *GeoRL*, **15**, 1333
- Futaana, Y., Machida, S., Saito, Y., Matsuoka, A., & Hayakama, H. 2003, *JGRA*, **108**, 1025
- Garrick-Bethell, I., & Kelley, M. R. 2019, *GeoRL*, **46**, 5065
- Garrick-Bethell, I., Poppe, A. R., & Fatemi, S. 2019, *GeoRL*, **46**, 5778
- Garrick-Bethell, I., Weiss, B. P., Shuster, D. L., & Buz, J. 2009, *Sci*, **323**, 356
- Garrick-Bethell, I., Weiss, B. P., Shuster, D. L., Tikoo, S. M., & Tremblay, M. M. 2017, *JGRE*, **122**, 76
- Green, J., Draper, D., Boardsen, S., & Dong, C. 2020, *SciA*, **6**, eabc0865
- Grimberg, A., Baur, H., Bochsler, P., et al. 2006, *Sci*, **314**, 1133
- Grimm, R. E., & Delory, G. T. 2012, *AdSpR*, **50**, 1687
- Güdel, M. 2020, *SSRv*, **216**, 143
- Halekas, J. S., Bale, S. D., Mitchell, D. L., & Lin, R. P. 2005, *JGR*, **110**
- Halekas, J. S., Brain, D. A., & Holmström, M. 2014a, in *Magnetotails in the Solar System*, ed. A. Keiling et al. (Washington, DC: AGU), 149
- Halekas, J. S., Brain, D. A., Mitchell, D. L., Lin, R. P., & Harrison, L. 2006, *GeoRL*, **33**, L08106
- Halekas, J. S., Lin, R. P., & Mitchell, D. L. 2003, *M&PS*, **38**, 565
- Halekas, J. S., Poppe, A. R., Lue, C., Farrell, W. M., & McFadden, J. P. 2017, *JGRA*, **122**, 6240
- Halekas, J. S., Poppe, A. R., McFadden, J. P., et al. 2014b, *GeoRL*, **41**, 7436
- Heber, V. S., Baur, H., & Wieler, R. 2001, in *AIP Conf. Proc. 598, Solar and Galactic Composition: A Joint SOHO/ACE Workshop* (Melville, NY: AIP), 387
- Heber, V. S., Baur, H., & Wieler, R. 2003, *ApJ*, **597**, 602
- Hefiti, S., Grünwaldt, H., Ipavich, F. M., et al. 1998, *JGR*, **103**, 29697
- Hennecke, E. W., & Manuel, O. K. 1977, *E&PSL*, **36**, 29
- Hijazi, H., Bannister, M. E., Meyer, H. M., III, et al. 2014, *JGRA*, **119**, 8006
- Holmström, M., Fatemi, S., Futaana, Y., & Nilsson, H. 2012, *EP&S*, **64**, 237
- Hood, L. L. 2011, *Icar*, **211**, 1109
- Jia, X., Slavin, J. A., Gombosi, T. I., et al. 2015, *JGRA*, **120**, 4763
- Jia, X., Slavin, J. A., Poh, G., et al. 2019, *JGRA*, **124**, 229
- Jian, L. K., Russell, C. T., & Luhmann, J. G. 2011, *SoPh*, **274**, 321
- Johnson, C. L., Purucker, M. E., Korth, H., et al. 2012, *JGRD*, **117**, D00U24
- Joy, K. H., Kring, D. A., Bogard, D. D., McKay, D. S., & Zolensky, M. E. 2011, *GeoCoA*, **75**, 7208
- Kallio, E. 2005, *GeoRL*, **32**, L06107
- Kallio, E., Wurz, P., Killen, R., et al. 2008, *P&SS*, **56**, 1506
- Kasper, J. C., Stevens, M. L., Lazarus, A. J., Steinberg, J. T., & Ogilvie, K. W. 2007, *ApJ*, **660**, 901
- Keika, K., Kistler, L. M., & Brandt, P. C. 2013, *JGRA*, **188**, 4441
- Kerridge, J. F. 1993, *RvGeo*, **31**, 423
- Killen, R. M. 2002, *M&PS*, **37**, 1223
- Kivelson, M. G., Wang, Z., Joy, S., et al. 1995, *AdSpR*, **16**, 59
- Klida, M. M., & Fritz, T. A. 2009, *AnGeo*, **27**, 4305
- Lu, Q. M., & Wang, S. 2005, *GeoRL*, **32**, L03111
- Lue, C., Futaana, Y., Barabash, S., et al. 2014, *JGRE*, **119**, 968
- Manka, R. H., & Michel, F. C. 1970, *Sci*, **169**, 278
- Massetti, S., Orsini, S., Milillo, A., et al. 2003, *Icar*, **166**, 229
- Massetti, S., Orsini, S., Milillo, A., & Mura, A. 2007, *P&SS*, **55**, 1557
- McGregor, S. L., Hughes, W. J., Arge, C. N., Owens, M. J., & Odstrcil, D. 2011, *JGRA*, **116**, A03101
- Meshik, A., Hohenberg, C., Pravidtseva, O., & Burnett, D. 2014, *GeoCoA*, **127**, 326
- Mighani, S., Wang, H., Shuster, D. L., et al. 2020, *SciA*, **6**, eaax0883
- Mitchell, D. L., Halekas, J. S., Lin, R. P., et al. 2008, *Icar*, **194**, 401
- Motschmann, U., & Glassmeier, K.-H. 1993, *GeoRL*, **20**, 987
- Nichols, R. H., Hohenberg, C. M., & Olinger, C. T. 1994, *GeoCoA*, **58**, 1031
- Nishino, M. N., Fujimoto, M., Saito, Y., et al. 2013, *P&SS*, **87**, 106
- Ó Fionnagáin, D., & Vidotto, A. A. 2018, *MNRAS*, **476**, 2465
- Omid, N., Blanco-Cano, X., Russell, C. T., Karimabadi, H., & Acuna, M. 2002, *JGRA*, **107**, 1487
- Oran, R., Weiss, B. P., Shprits, Y., Milijkočić, K., & Tóth, G. 2020, *SciA*, **6**, eabb1475
- Ozima, M., Seki, K., Terada, N., et al. 2005, *Natur*, **436**, 655
- Pepin, R. O., Becker, R. H., & Rider, P. E. 1995, *GeoCoA*, **59**, 4997
- Pepin, R. O., Becker, R. H., & Schlutter, D. J. 1999, *GeoCoA*, **63**, 2145
- Pepin, R. O., Nyquist, L. E., Phinney, D., & Black, D. C. 1970, *LPSC*, **2**, 1435
- Plainaki, C., Massetti, S., Jia, X., et al. 2020, *ApJ*, **900**, 74
- Podosek, F. A., Huneke, J. C., Burnett, D. S., & Wasserburg, G. J. 1971, *E&PSL*, **10**, 199
- Pognan, Q., Garraffo, C., Cohen, O., & Drake, J. J. 2018, *ApJ*, **856**, 53
- Poppe, A. R., Fatemi, S., Halekas, J. S., Holmström, M., & Delory, G. T. 2014, *GeoRL*, **41**, 3766
- Poppe, A. R., Fatemi, S., & Khurana, K. K. 2018, *JGRA*, **123**, 4614
- Poppe, A. R., Fillingim, M. O., Halekas, J. S., Raeder, J., & Angelopoulos, V. 2016, *GeoRL*, **43**, 6749
- Purucker, M. E. 2008, *Icar*, **197**, 19
- Raines, J. M., DiBraccio, G. A., Cassidy, T. A., et al. 2015, *SSRv*, **192**, 91
- Raines, J. M., Gershman, D. J., Slavin, J. A., et al. 2014, *JGRA*, **119**, 6587
- Raines, J. M., Gershman, D. J., Zurbuchen, T. H., et al. 2013, *JGRA*, **118**, 1604
- Reynolds, J. H., Hohenberg, C. M., Lewis, R. S., Davis, P. K., & Kaiser, W. A. 1970, *Sci*, **167**, 545
- Russell, C. T., Coleman, P. J., Jr., Lichtenstein, B. R., & Schubert, G. 1973, *LPSC*, **3**, 2833
- Saito, Y., Miyashita, Y., Fujimoto, M., et al. 2008, *GeoRL*, **35**, L07103
- Sarantos, M., Killen, R. M., Glenar, D. A., Benna, M., & Stubbs, T. J. 2012, *JGR*, **117**
- Seki, K., Terada, N., Yagi, M., et al. 2013, *JGRA*, **118**, 3233
- Shea, E. K., Weiss, B. P., Cassata, W. S., et al. 2012, *Sci*, **335**, 453
- Shimazu, M. 2001, *JGR*, **106**, 8333
- Sibeck, D. G., McEntire, R. W., Lui, A. T. Y., et al. 1987, *JGR*, **92**, 12097
- Simon, S., Bagdonat, T., Motschmann, U., & Glassmeier, K.-H. 2006, *AnGeo*, **24**, 407
- Slavin, J. A., Middleton, H. R., Raines, J. M., et al. 2019, *JGRA*, **124**, 6613
- Sorathia, K. A., Merkin, V. G., Ukhorskiy, A. Y., Mauk, B. H., & Sibeck, D. G. 2017, *JGRA*, **122**, 9329
- Terada, K., Yokota, S., Saito, Y., et al. 2017, *NatAs*, **1**, 0026
- Tikoo, S. M., Weiss, B. P., Cassata, W. S., et al. 2014, *E&PSL*, **404**, 89
- Tikoo, S. M., Weiss, B. P., Shuster, D. L., et al. 2017, *SciA*, **3**, e1700207
- Tsubouchi, K., Nagai, T., & Shinohara, I. 2016, *JGRA*, **121**, 1233
- Vernisse, Y., Krieger, H., Wiehle, S., Motschmann, U., & Glassmeier, K.-H. 2013, *P&SS*, **84**, 37
- Vogel, N., Heber, V. S., Baur, H., Burnett, D. S., & Wieler, R. 2011, *GeoCoA*, **75**, 3057
- von Steiger, R., Schwadron, N. A., Fisk, L. A., et al. 2000, *JGR*, **105**, 27217
- Vorburger, A., Wurz, P., Barabash, S., et al. 2014, *JGRA*, **119**, 709
- Walker, R. J., Richard, R. L., & Ashour-Abdalla, M. 2013, *GMS*, **90**, 311
- Walsh, B. M., Ryou, A. S., Sibeck, D. G., & Alexeev, I. I. 2013, *JGRA*, **118**, 1992
- Wang, Y.-C., Müller, J., Ip, W.-H., & Motschmann, U. 2011, *Icar*, **216**, 415
- Wei, Y., Zhong, J., Hui, H., et al. 2020, *GeoRL*, **47**, e86208
- Weiss, B. P., & Tikoo, S. M. 2014, *Sci*, **346**, 1198
- Wieler, R. 1998, *SSRv*, **85**, 303
- Wieler, R. 2016, *ChEG*, **76**, 463
- Wieler, R., & Baur, H. 1995, *ApJ*, **453**, 987
- Wieler, R., Baur, H., & Signer, P. 1986, *GeoCoA*, **50**, 1997
- Wieler, R., Humbert, F., & Marty, B. 1999, *E&PSL*, **167**, 47
- Wieler, R., Kehm, K., Meshik, A. P., & Hohenberg, C. M. 1996, *Natur*, **384**, 46
- Wilson, L. B., III, Stevens, M. L., Kasper, J. C., et al. 2018, *ApJS*, **236**, 41
- Winslow, R. M., Johnson, C. L., Anderson, B. J., et al. 2012, *GeoRL*, **39**
- Winslow, R. M., Johnson, C. L., Anderson, B. J., et al. 2014, *GeoRL*, **41**, 4463
- Wood, B. E., Müller, H.-R., Zank, G. P., Linksy, J. L., & Redfield, S. 2005, *ApJL*, **628**, L143
- Wurz, P., Rohner, U., Whitby, J. A., et al. 2007, *Icar*, **191**, 486
- Yagi, M., Seki, K., Matsumoto, Y., Delcourt, D. C., & Leblanc, F. 2010, *JGRA*, **115**, A10253
- Yagi, M., Seki, K., Matsumoto, Y., Delcourt, D. C., & Leblanc, F. 2017, *JGRA*, **122**, 10990
- Zelenyi, L., Oka, M., Malova, H., et al. 2007, *SSRv*, **132**, 593
- Zhang, H., Khurana, K. K., Kivelson, M. G., et al. 2014, *JGRA*, **119**, 5220
- Zurbuchen, T. H., Raines, J. M., Slavin, J. A., et al. 2011, *Sci*, **333**, 1862